

Supporting Information for “Scratch-Resistant Sapphire Nanostructures with Anti-Glare, Anti-Fogging, and Dust-Mitigation Properties”

Kun-Chieh Chien,¹ Mehmet Kepenekci,¹ Andrew Tunell, and Chih-Hao Chang*

Walker Department of Mechanical Engineering, The University of Texas at Austin,

Austin, Texas, 78712, United States

*Corresponding email: chichang@utexas.edu

¹These authors contributed equally to this work

Supporting Information A: Fabrication of Sapphire Nanostructures

The proposed bio-inspired sapphire nanostructures are fabricated using a combination of interference lithography (IL) and reactive ion etching (RIE) on both sides of a sapphire substrate, as illustrated in Fig. S1. First, as shown in Fig. S1(a), a thick polysilicon layer with a thickness of approximately 1 μm is deposited on both sides of the sapphire substrate through low-pressure chemical vapor deposition (LPCVD). Subsequently, a 100 nm anti-reflection coating (ARC, i-con-7, Brewer Science) and a 200 nm photoresist (PFI-88A2, Sumitomo) are spin-coated onto the polysilicon layer. The antireflection coating is employed to minimize the reflection from the polysilicon layer and reduce standing waves and sidewall waviness during the IL process. Lloyd's mirror IL with two orthogonal exposures is utilized to pattern 2D pillar arrays with a period of 300 nm in the photoresist, as illustrated in Fig. S1(b). Note this step can also be patterned using other lithography techniques such as nanoimprint lithography.

The resist pattern is transferred into the ARC layer using O_2 RIE (RF power 60 W, pressure 13 mTorr, flow rate 25 sccm), after which HBr RIE (RF power 20 W, ICP power 200 W, pressure 8 mTorr, flow rate 20 sccm) is used to etch into the polysilicon mask layer. The low RF power increases the silicon to photoresist etch selectivity and creates high aspect-ratio pillar arrays as an etch mask for the subsequent sapphire etching process, as shown in Fig. S1(c). The pattern is transferred into the substrate using BCl_3/HBr RIE (RF power 400 W, ICP power 1500 W, pressure 8 mTorr, flow rate 15 sccm for each gas), resulting in sapphire nanostructures with a tapered profile, as depicted in Fig. S1(d). A hard polymer film (ProTEK B3-25, Brewer Science) is applied to the front side through spin-coating to protect the nanostructures, as illustrated in Fig. S1(e). The fabrication process from Figure S1(a)-S1(d) is repeated to pattern the backside of the sapphire substrate. After completing the fabrication on the other side of the sapphire substrate, the

protective film can be removed using a solvent solution (ProTEK Remover 100, Brewer Science) and then cleaned through O₂ plasma etching. Consequently, the sapphire substrate with bio-inspired nanostructures on both sides is shown in Fig. S1(f).

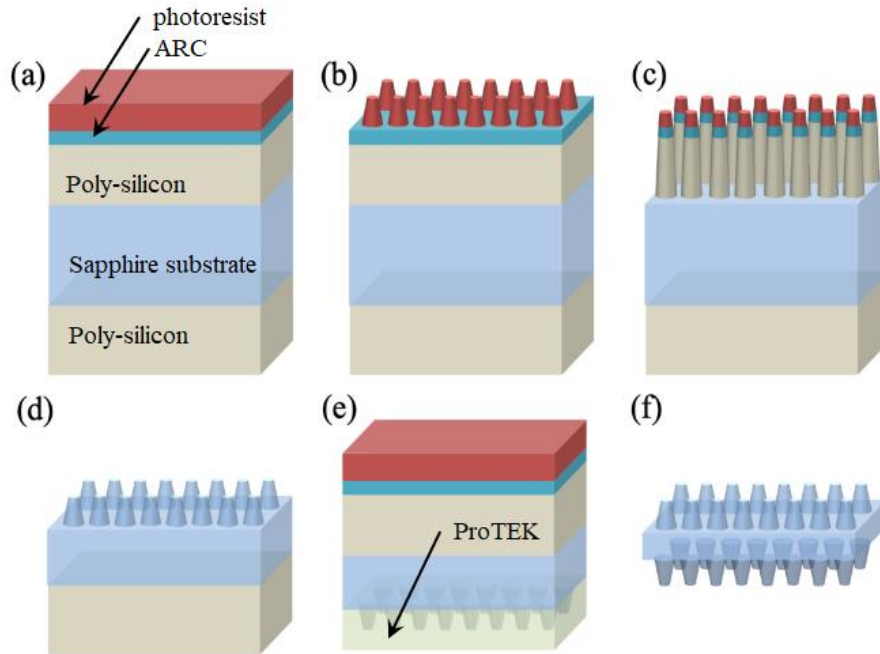


Fig. S1 Schematic of the fabrication process for bio-inspired sapphire nanostructures. (a) Polysilicon LPCVD on both sides, followed by the spin coating of anti-reflection coating and photoresist. (b) Patterning 2D pillar arrays with a period of 300 nm in photoresist using Lloyd's mirror IL. (c) Transferring the pattern into the polysilicon layer using O₂ RIE and HBr RIE with low RF power, forming high aspect-ratio (HAR) periodic pillars as the etch mask. (d) Etching the sapphire substrate to form bio-inspired sapphire nanostructures using BCl₃/HBr RIE. (e) Applying a protective polymer film to the patterned side, followed by the same fabrication process shown in (a) to (d). (f) Double-sided patterned sapphire sample.

Fig. S2 shows a SEM image of high aspect-ratio pillar arrays consisting of polysilicon, anti-reflection coating, and photoresist, with a total height of approximately 1.27 μm. These nanopillars serve as an etch mask for transferring the pattern into the sapphire substrate. As a result, bio-inspired tapered sapphire nanostructures with a height of 500 nm can be obtained, as shown in Fig. 1 in the main text.

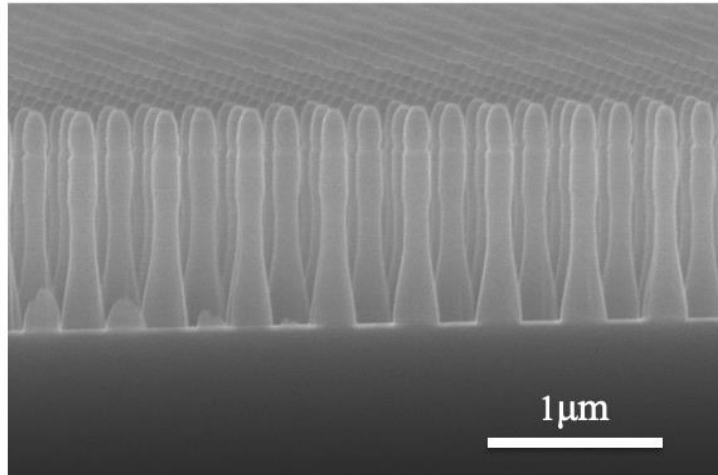


Fig. S2 Nanopillars consisted by polysilicon, antireflection coating, and photoresist, which will be served as an etch mask for the sapphire etching process.

Supporting Information B: Optical Modeling

The sapphire nanostructures is modeled using rigorous coupled-wave analysis (RCWA) code developed in-house and implemented using Matlab. In this model the tapered sapphire nanostructures are approximated by discrete 2D gratings and varying duty cycle. Each grating layer consists of a square lattice with the same period (Λ) and duty cycle (f) in x and y directions. The index of the sapphire varies with the incident wavelength and is modeled using the material dispersion of sapphire in published data. The cross-section SEM image of the sapphire substrate is used to model the duty cycle of each layer, as shown in Figure S3.

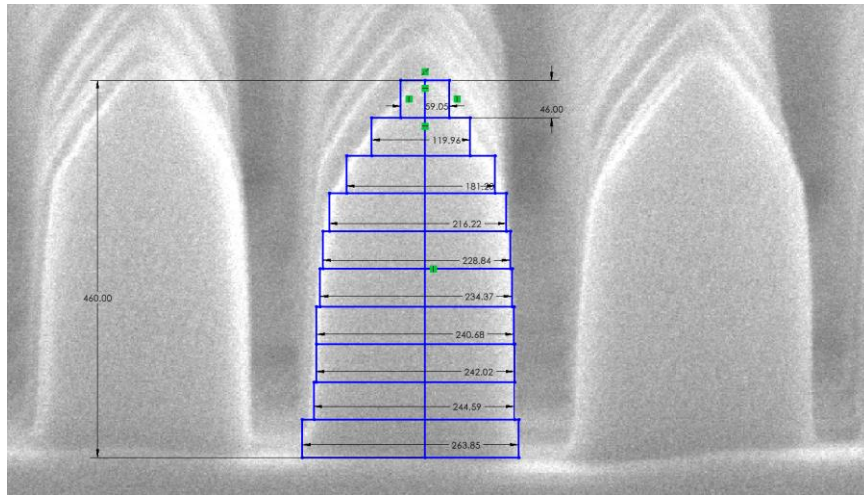


Figure S3. Cross-section SEM image of the nanostructures at a 20 degree tilt.

Table S1. Geometry of the 10 discretized layers used to model the sapphire nanostructures

Layer	Measurements (nm)	Thickness (nm)	Duty-Cycle
1	59.0	46	0.032
2	120.0	46	0.132
3	181.2	46	0.302
4	216.2	46	0.429
5	228.8	46	0.481
6	234.4	46	0.504
7	240.7	46	0.532
8	242.0	46	0.538
9	244.6	46	0.549
10	263.9	46	0.639

The geometry of the 10 discretized layers of the nanostructure is shown in Table S1. Using these parameters, the transmittance of the nanostructures at a single air/sapphire interface is calculated and compared with the planar interface. The double-sided transmittance is calculated by square of the single interface transmittance to account for both sides. The single-sided transmittance is calculated by the product of the transmittance of the nanostructures and planar interfaces. The double-sided, single-sided, and planar sapphire transmittance are plotted in Figure 2(a) of the main text with the experimental data. The transmission of the samples versus angle is also calculated using the RCWA model, as plotted in Figure 2(b) of the main text.

The RCWA model is also used to examine the effect of the 330 nm period on the short wavelength band of the transmittance, which is around 550 nm. As discussed in the main text of the manuscript this bound can be attributed to the period and scales with $\lambda_{min} = \Lambda(n_s + \sin \theta_i)$. The shorter wavelength bound can be extended by using smaller period structures, and would yield $\lambda_{min} = 350$ nm for $\Lambda = 200$ nm. This effect is shown in the modeled transmission for a 200 nm period sapphire structures, as shown in Figure S4.

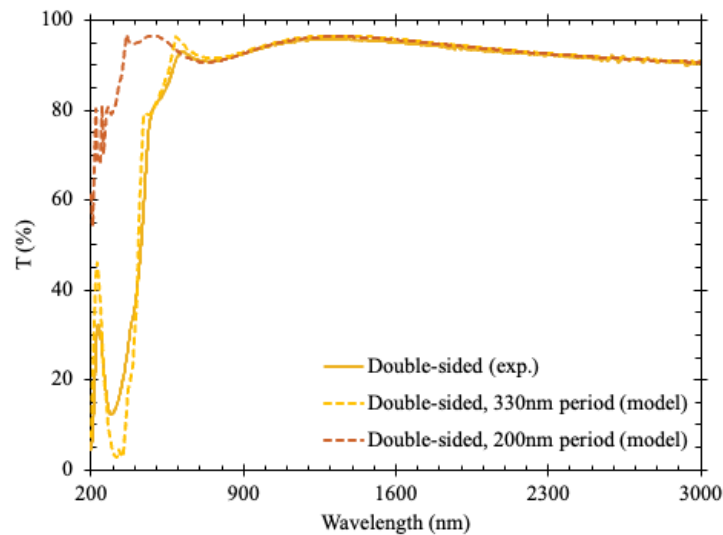


Figure S4. Simulated transmission for sapphire nanostructures with 200 nm period.

Supporting Information C: Contact Angle Measurement

The water contact angles of the nanostructured and planar sapphire samples with a silane treatment are measured to quantify the surface wetting. Based on intermolecular interactions, high surface energy leads to a low contact angle, while low surface energy results in a high contact angle. In this experiment, both static and dynamics contact angles are measured using the FTA200 goniometer (First Ten Angstroms). Each sample is placed horizontally on the stage in front of an optical microscope. For the static contact angle measurements, a single water droplet is deposited on the surface using a syringe. For the dynamic contact angle measurement, multiple water droplets are added to or removed from the surface using a syringe. Goniometer results are shown in Fig. S5. The water contact angle of the treated planar sapphire surface can be increased to 98.9° since the sapphire surface energy is decreased by coating a monolayer of silane on the surface, as shown in Fig. S5(a). Furthermore, the water contact angle of the nanostructured sapphire surface can be further increased to 144.2° due to the increase in surface roughness, as shown in Fig. S5(b). Moreover, Fig. S5(c) shows the advancing angle being measured as water is added to the existing water droplet, and Fig. S5(d) shows the receding angle being measured as water is removed from the existing water droplet. Therefore, the measured advancing and receding angles are 135.0° and 128.2° , respectively, resulting in a water contact angle hysteresis of 12.2° . In comparison, the advancing and receding angles are 103.8° and 77.7° for the planar sapphire sample, respectively, resulting in a contact angle hysteresis of 26.3° . These data are summarized in the following Table S2.

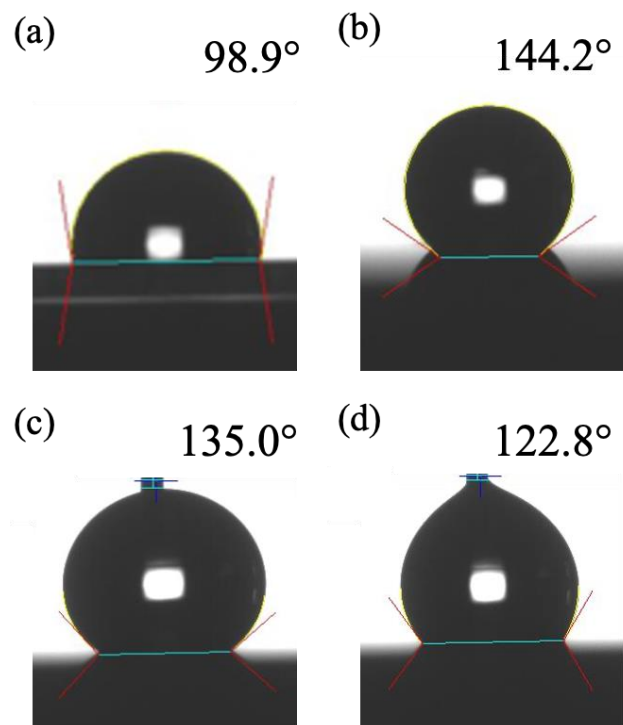


Fig. S5. Water contact angle of silane treated (a) planar sapphire surface and (b) the nanostructured sapphire surface. (c) The advancing water contact angle when adding water into the water droplet. (d) The receding water contact angle when removing water from the water droplet.

Table S2. Wetting measurement for the planar and nanostructured sapphire surfaces.

Measurements	Planar Sapphire	Nanostructured Sapphire
Static contact angle	98.9°	144.2°
Advancing angle	103.8°	135.0°
Receding angle	77.7°	122.8°
Contact angle hysteresis	26.1°	12.2°

Supporting Information D: Dust Mitigation Properties

Particle adhesion forces have been shown to be strongly dependent on the surface geometry. This geometry affects the contact area between the surface and particle resting on it, causing the adhesion force to scale with the area in contact. This effect can be described by the Johnson-Kendall-Roberts (JKR) model, where the adhesion force between two spherical objects with radii R_1 and R_2 is given as,

$$F_{adh} = \frac{3}{2} \pi f \frac{R_1 R_2}{R_1 + R_2} \Delta\gamma \quad (\text{S.1})$$

Where f is the fractional contact area due to nanoscale surface roughness, $\Delta\gamma$ is the work of adhesion, and R_1 and R_2 are the radii of the nanostructure and contacting dust particle, respectively. Here it can be observed that for nanostructures with sharp features that are much smaller than the particle size, or $R_1 \ll R_2$, the adhesion force becomes,

$$F_{adh} = \frac{3}{2} \pi f R_2 \Delta\gamma \quad (\text{S.2})$$

Which scales $F_{adh} \sim f R_2 \Delta\gamma$. The tip of the fabricated sapphire nanostructures is sharp and has $R_1 \sim 30$ nm, which can be effective mitigating the adhesion of microscale dust particles where $R_2 > 1$ μm . Therefore, the geometry of the nanostructured sapphire leads to a significant reduction in the adhesion forces. Further refinements to the surface were made to enhance the dust mitigating performance. This includes an addition of trichloro(octyl)silane which reduces the surface energy, $\Delta\gamma$, as confirmed by the contact angle measurements of the sample in the previous section. The fractional contact area due to nanoscale surface roughness is not measured for the sapphire sample but have been determined in past experiments to be around 0.1.

The results of the dust adhesion forces are evaluated experimentally using a lunar dust simulant obtained from Exolith Labs (Exolith, LMS-1 Lunar Mare Simulant). The dusts are dispensed onto both the nanostructured and planar sapphire samples using a spoon while mounted together on a horizontal stage to create a coating of approximately 2-5 mm thick. The stage was then rotated 90°, slowly by hand, until the samples are aligned vertically, and the loose dust was removed by gravity alone. This process is documented in the supplementary video showing the samples mounted, the removal by gravity, and the resulting difference in residual dust after tilting vertically.

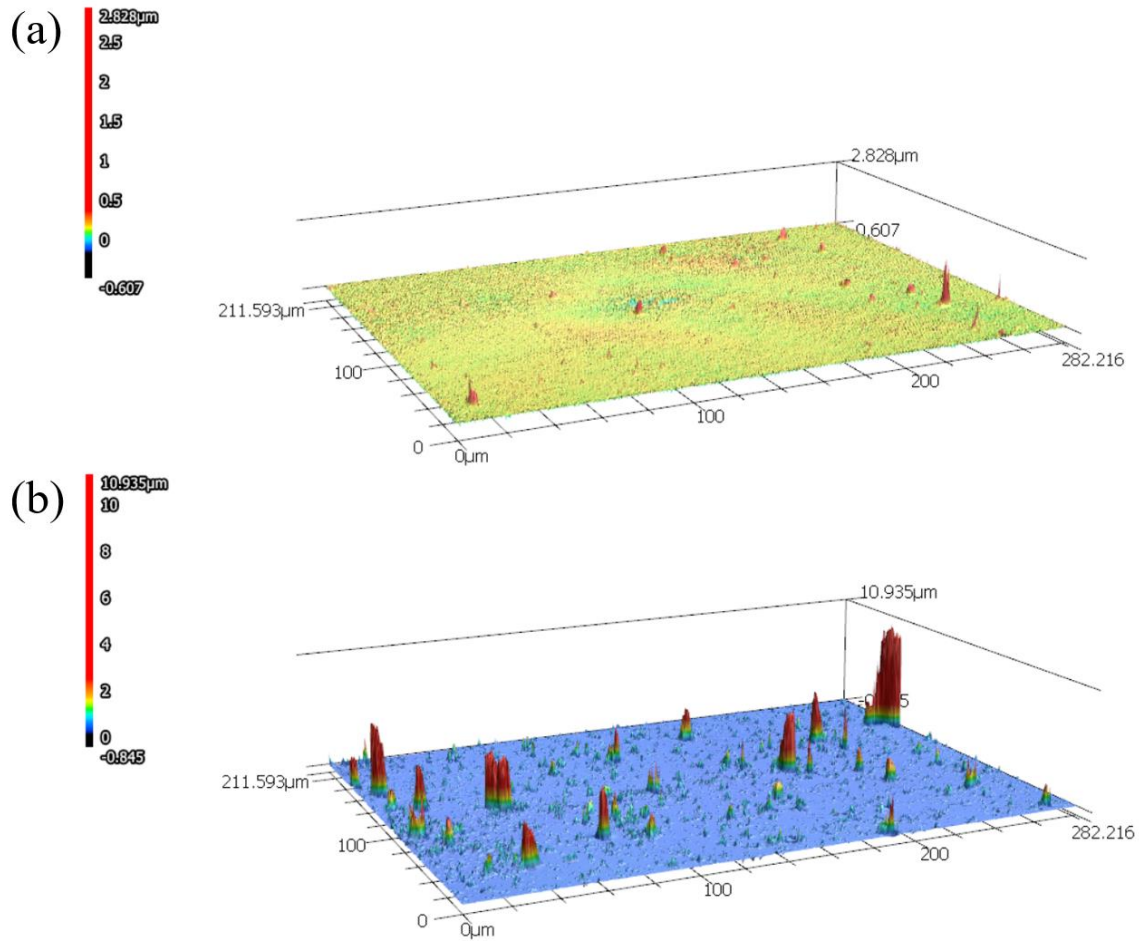


Fig. S6. Confocal scans of (a) nanostructured sapphire surface and (b) planar sapphire surface after following dust application and removal by gravity.

The quantity of residual dust was then evaluated by confocal microscopy using a Keyence VK-X1100 Optical Profilometer. This creates three dimensional scans of the surface topography, as shown in Fig. S6, that allow for the detection of dust as any raised point above the substrate. Through an analysis of 15 randomly located height map that is 211 μm by 282 μm area scans on each of the nanostructured and planar substrates, the percent surface area covered by dust was found. The standard deviation of these 15 values was taken to calculate the error bar. This analysis resulted in $31.8 \pm 2.7\%$ and $1.3 \pm 0.8\%$ for the reference planar and nanotextured sapphire samples respectively. The percentage improvement of the dust mitigating properties was also evaluated using the following formula, $\% \textit{Improvement} = (A_{\textit{nano}} - A_{\textit{planar}})/A_{\textit{planar}}$. Here the $A_{\textit{nano}}$ and $A_{\textit{planar}}$ values were determined by confocal microscopy and refer to the percentage of the projected surface area of each substrate that was covered by dust. which resulted in a 95.9% reduction in residual dust coverage. Additional details extracted from the confocal area scans include the distribution of the residual dust which is presented in the main text.

Supporting Information E: Mechanical Testing of Sapphire Nanostructures

The nanoindentation tests were done using a conospherical indenter with 10 μm tip radius and 90° cone angle. All quasi-static tests are shown in Fig. S7, and a representative cyclic loading test with quantities used in calculations is shown in Fig. S8. The hardness and indentation modulus values were calculated using the Oliver-Pharr method as explained below. For quasi-static tests, the sample tested with different peak loads that produce maximum indentation depth in the region of 10-15% of the pillar height to avoid the substrate and densification effect at lower depth.

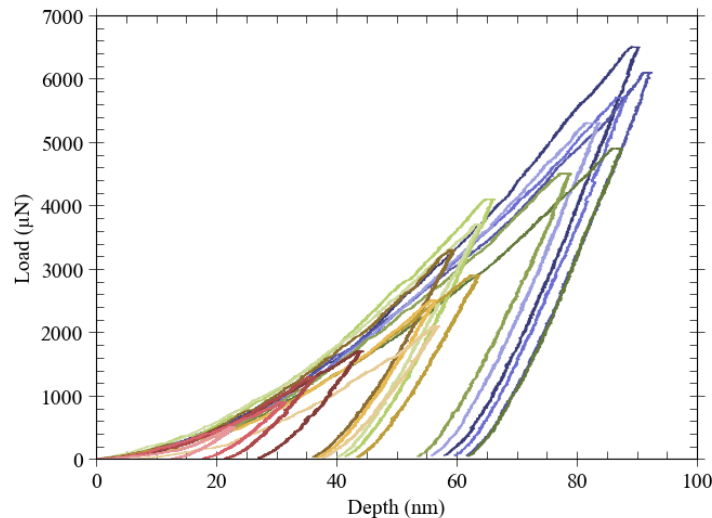


Fig. S7. Quasi-static nanoindentation tests of sapphire nanostructures.

The cyclic loading test was done at 16 different locations, using 10 partial loading and unloading segments, where the probe is unloaded up to 10% of the peak force value of the previous loading segment. This method provided 10 different data points for each test location. The hardness and elastic modulus with standard deviation values were calculated and used in Figure 8(b) and 8(c).

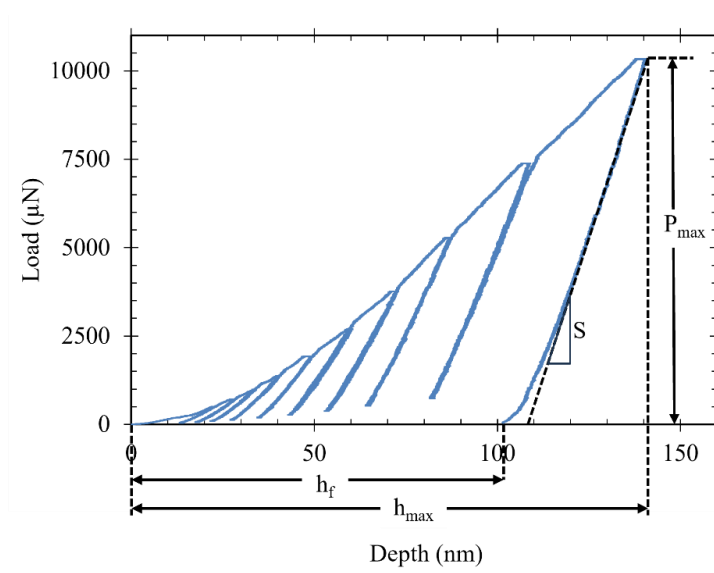


Fig. S8. A representative cyclic nanoindentation test of sapphire nanostructures.

The unloading curve could be approximated by following power law relation.

$$P = \alpha(h - h_f)^m \quad (\text{S.4})$$

where α and m are the power law fitting constants, h is the depth and h_f is the final depth. The unloading data between 20% and 95% of the maximum unloading load, P_{max} , was used to fit a curve in the form of Eq. S.4. The slope of the unloading curve, S , is calculated via the derivative of the above equation. Then, the sink-in depth h_s is calculated via Eq. S.5.

$$h_s = \epsilon \frac{P_{max}}{S} \quad (\text{S.5})$$

where ϵ is a constant depends on the indenter geometry. Then, the contact depth (h_c) is calculated using Eq. S.6.

$$h_c = h_{max} - \epsilon \frac{P_{max}}{S} \quad (S.6)$$

The cross-sectional area of the indenter could be approximated by using the contact depth to obtain tip area function as shown in Eq. S7.

$$A(h_c) = C_0 h_c^2 + C_1 h_c + C_2 h_c^{1/2} + C_3 h_c^{1/4} + C_4 h_c^{1/8} + C_5 h_c^{1/16} \quad (S.7)$$

The constants, C_n , were obtained empirically based on indentations of a fused silica surface. The fitted constants are given in Table S.3

Table S.3. Values of fitting constants

Constants	Fitted Constants
C_0	-3.141593
C_1	193006.518
C_2	-11177577.9
C_3	105428227.5
C_4	-254712610.1
C_5	161000362.4

Using the maximum load, P_{max} , and the tip area found using the contact depth and tip area function, hardness, H , can be calculated,

$$H = \frac{P_{max}}{A} \quad (S.8)$$

The indentation modulus, or reduced modulus, E_r , is calculated using Eq. S.9.

$$E_r = \frac{\sqrt{\pi}}{2} \frac{S}{\sqrt{A}} \quad (S.9)$$

The pencil hardness testing is performed using a pencil hardness tester that applies a 7.5N load at a constant angle 45°, with a 2B pencil. The sample then cleaned via sonication in deionized

water, then acetone and finally in isopropyl alcohol for 5 minutes each. Then the sample was subjected to piranha solution and followed by RCA clean at 70°C, and oxygen plasma cleaning for 15 minutes each. SEM images taken after cleaning show the sample is mostly free from pencil lead but there are pencil lead debris between nanopillars in some regions.